J Vis (2010) 13:347–353
DOI 10.1007/s12650-010-0053-y

REGULAR PAPER

Liyong Zou · Cangli Liu · Duowang Tan · Wenbin Huang · Xisheng Luo

On interaction of shock wave with elliptic gas cylinder

Received: 28 February 2010 / Revised: 11 June 2010 / Accepted: 28 August 2010 / Published online: 12 September 2010

Abstract The interaction of a planar shock with one elliptic heavy-gas (SF_6) cylinder surrounded by air is investigated experimentally. By changing the aspect ratio of the elliptic cylinder, the influence of the initial shape on the evolution of the interface is visualized by a series of dynamic photos utilized by a high-speed camera. It is found that the longer the axis perpendicular to the shock front, the faster and the severer the deformation of the gas cylinder. This can be explained mainly by the different amount of vorticity produced by the misalignment between the density gradient and the pressure gradient. When the vertical axis is much longer than the horizontal axis, the vorticity production is mainly concentrated at the upper and lower corners, which rolls up in time, and results in a structure of big vortex-pair. When the horizontal axis is much longer than the vertical axis, the baroclinic vorticity production distributes at almost every position along the interface, which leads to a faster rolling up of vortices, and even second vortex may develop at later times.

Keywords Flow visualization · Richtmyer–Meshkov instability · Elliptic gas cylinder · Shock wave

1 Introduction

When an interface between two fluids with different densities experiences an impulsive acceleration, the perturbations of the interface will grow, which is called the Richtmyer–Meshkov instability (RMI) (Meshkov 1969; Richtmyer 1960). This instability occurs in a wide range of applications such as supernova (Arnett et al. 1989), inertial confined fusion (Lindl et al. 1992), deflagration to detonation transition (Markstein 1957), etc. Therefore, it has been extensively investigated in the past two decades by means of experimental, numerical and theoretical methods. Surveys are given by Brouillette (2002) and Zabusky (1999).

The interaction of a shock wave with a gas cylinder can be regarded as one common test problem for the study of the RMI. The shock wave provides the impulsive impact on the interface which is formed either by a cylindrical bubble (Haas and Sturtevant 1987) or by a gas cylinder (Tomkins et al. 2002, 2008). This

L. Zou · C. Liu · D. Tan · W. Huang
National Key Laboratory of Shock Wave and Detonation Physics,
Institute of Fluid Physics, CAEP, Mianyang 621900, People's Republic of China
Tel.: +86-816-2490590
Fax: +86-816-2485139

X. Luo (✉)
Department of Modern Mechanics, University of Science and Technology of China,
Hefei 230026, People's Republic of China
E-mail: xluo@ustc.edu.cn
Tel.: +86-551-3603390
Fax: +86-551-3606457

problem has been examined experimentally (Haas and Sturtevant 1987; Jacobs 1993; Prestridge et al. 2000) and computationally (Quirk and Karni 1996). This gas-cylinder problem can also be served as a good benchmark for code validation because it exhibits complex and non-linear behaviors in a very simple initial configuration (Zoldi 2002).

The evolution of the interface after the sudden impact of the shock is mainly related to two mechanisms, the baroclinic vorticity deposition (Jacobs 1993) and the pressure perturbation (Haas and Sturtevant 1987). The baroclinic vorticity is generated where the pressure gradient is misaligned with the density gradient. The pressure perturbation is caused by the wave phenomena including the shock focusing. Both mechanisms strongly depend on the initial shape of the gas cylinder. In the present work, we performed an experimental investigation of the interaction of a planar shock with one elliptic heavy-gas (SF_6) cylinder surrounded by air. By changing the axis ratio of the elliptic cylinder, the influence of the initial shape on the evolution of the interface can be studied. In fact, the circular gas cylinder can be considered as a special case of the elliptic cylinder.

2 Experimental facility and method

2.1 Facility

All experiments for this study are carried out in a stainless-steel shock tube IFP50 with a length of 4.7 m and a square cross-sectional area of 50 × 50 mm^2. As shown in Fig. 1, it consists of a driver section, a driven section and a test section. The driver section is movable and has a length of 1.03 m. The driven section is fixed and has a length of 3.02 m. The test section is 0.65 m long and has four optical windows (250 × 50 mm^2). To generate a shock wave, the driver chamber is slowly filled with nitrogen until a plastic membrane, separating the driver chamber from the driven chamber, is ruptured. Both driven chamber and test chamber are initially at ambient pressure. In this case, an incident shock wave of Mach number 1.25 can be produced with a repeatability of the shock speed typically within ±2%.

2.2 Elliptic gas cylinder creation

The method of the gas cylinder creation is similar to the one used in Tomkins et al. (2003, 2008) and Jacobs (1993). Supplied from a high-pressure bottle and monitored by a rotameter and a needle valve, SF_6 gas is introduced into a chamber placed above the test section of the shock tube. When the volume fraction of the SF_6 in the chamber is larger than 98% (monitored by a SF_6 gas analyzer FT-103P), glycol fog droplets, created with a theatrical fog machine, are then transferred into the chamber and mixed with the heavy gas for the purpose of visualization. In order to have a good mixing with the heavy gas, the injection nozzle of the fog locates at the bottom of the sidewall of the chamber. It should be pointed out that the volume fraction of the glycol fog droplets in the heavy gas is about $1:10^5$, which means that adding the glycol fog droplets has a negligible influence on the heavy gas density (less than 0.1%). The fog droplets have the typical sizes in the order of 0.5 μm in diameter, and the flow-tracking fidelity has been analyzed by Rightley et al. (1997, 1999) and Prestridge et al. (2000) in the similar shock acceleration system. It should be noted that, although the dynamic particle tracking is good using this diagnostic, the precise edges of the cylinder are not known

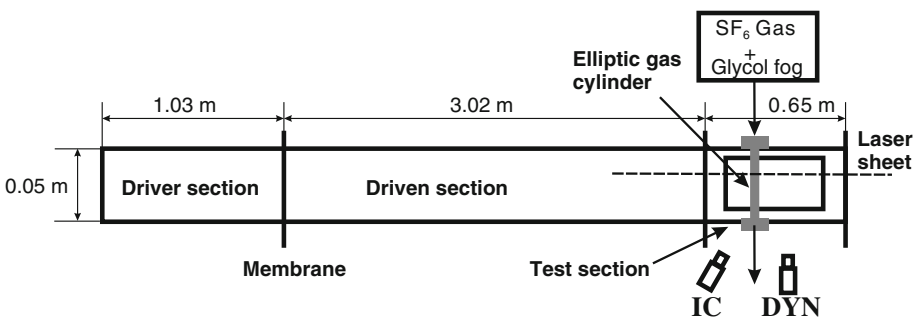

Fig. 1 Schematic of the shock tube IFP50 with peripheral devices. *IC* camera for taking the initial shape of the gas cylinder, *DYN* high-speed camera for taking dynamic photos of the gas cylinder

because diffusion dominates the initial conditions of the cylinder, and the SF6 diffuses faster than the fog (Goodenough et al. 2005).

A stainless-steel tube connects the chamber to the insert fitted on the upper wall of the test section. The insert with the desired elliptic nozzle is modular and can be interchanged easily for all nozzles. Thus, the configuration of elliptic gas-cylinder may be changed by simply switching inserts. Because SF_6 is five times denser than air, the gas–fog mixture flows into the test section from the chamber along the nozzle driven by gravity. A mild suction through an exhaust plenum at the bottom of the test section extracts the SF_6 gas seeded with glycol fog out of the shock tube. The suction is carefully controlled and adjusted to obtain the initial elliptic gas-cylinder in a steady, repeatable way. Compared with the speed of the shock ($\approx$420 m/s) or the convective velocity of the SF_6 gas ($\approx$100 m/s), the vertical flow velocity ($\approx$0.15 m/s) is very small and insignificant, thus ensuring the quasi-two-dimensional nature in the visualization plane.

A top view of the cross-section of the elliptic cylinder configuration just prior to the shock impact is shown schematically in Fig. 2. The initial geometry of the gas-cylinder in the test section depends upon the shape of the output orifice, which is a series of elliptic cross-section. In the present work, as listed in the Table 1, experiments are performed at different ratios of x-axis over y-axis of the ellipse, $a/b = 4/1$, 3/1, 2/1, 1/1, 1/2, 1/3 and 1/4 with a and b denoting the elliptic axis in x- and y-directions, respectively. For all cases, the area of the ellipse $0.25\pi ab$ keeps a constant 19.63 mm^2. Figure 3 shows a picture of the initial elliptic SF_6 cylinder taken along the axial direction of shock tube in a typical shot. Due to the diffuse effect of the gas cylinder that occurs immediately below the nozzle, the real sizes of a and b are slightly larger than that of the nozzle geometry as measured from the initial condition image. This certainly reduces the density gradient too. By measuring the size of the ellipse, the diffuse layer has a thickness of 10% of the nozzle size at the observing plane, i.e. 20 mm below the nozzle exit.

2.3 Diagnostics

The shock tube is equipped with six ports. Four of them are used to flush mount piezoelectric pressure transducers (PCB M113A26) on the wall of driven section. Other ports are used to inject or extract the test gas.

As shown in Figs. 1 and 3, the flow is illuminated by a 10-W constant illumination laser (Coherent Company, Verdi-V10) with a wavelength of 532 nm. The beam is transformed into a thin ($\approx$1 mm) horizontal laser sheet by using a set of lenses. The light sheet enters into the test section at about 20 mm below the nozzle exit and allows CCD camera to image the evolution of the elliptic cylinder. The trigger of CCD camera depends on a pressure transducer at the downstream end of the driven section of the shock tube.

All the images are captured using two independent cameras. The initial condition images, immediately prior to shock impact, are captured with a Photron Fastcam SA1.1 camera (IC in Fig. 1), which is inclined at 60° to the laser sheet. Images of IC camera are re-mapped to compensate the distortion effect caused by the inclination. The mapping coefficient is acquired by comparing a distorted picture of a test grid with the undistorted picture of the same grid.

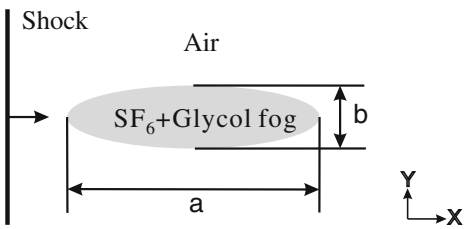

Fig. 2 Schematic of one elliptic cylinder. The ratio a/b ranges from 4 to 0.25

Table 1 Experimental parameters in different cases

Case	1	2	3	4	5	6	7
a (mm)	10.0	8.7	7.0	5.0	3.5	2.9	2.5
b (mm)	2.5	2.9	3.5	5.0	7.0	8.7	10.0
a/b	4	3	2	1	0.5	0.33	0.25

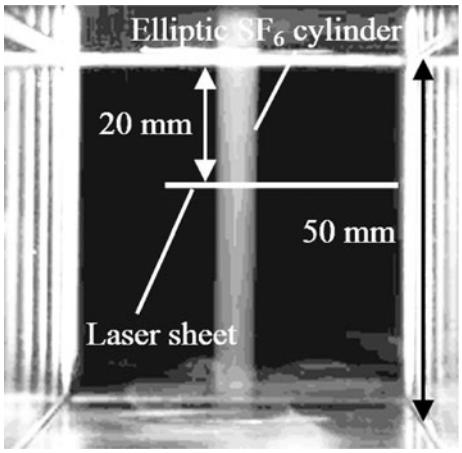

Fig. 3 Photograph showing initial gas-cylinder seeded with glycol fog

The evolution images during the post-shock flow are obtained by a Photron Fastcam-APX RS camera (DYN in Fig. 1) which is oriented orthogonally to the plane of the laser sheet. The duration of the five exposures on the CCD is 2 μs, which produces reasonable image quality at 20 μJ of optical energy. All the images are acquired before the shock reflected from the end wall or the rarefaction from the driver section reaches the test section. A frame rate of 10^4 fps is used, which corresponds to an image size of 640 × 384 pixels. These images give a resolution of 138 μm/pixel. As mentioned before, the sizes of fog tracer particles are in the order of 0.5 μm in diameter. Because these particles are much larger than SF_6 gas molecules, they scatter planar laser light much more efficiently, enabling the camera to collect images of local fog particle concentration, which in the post-shock flow is proportional to the actual gas density.

3 Results and discussion

The evolution images of all the seven cases are shown in Fig. 4. Cases 1–7 correspond to the rows from top to bottom, respectively. As mentioned before, the initial images obtained from IC camera have been corrected. It should be pointed out that images from 0 to 0.2 ms are not available because the gas-cylinder creator blocks the view of the camera during that period. Therefore, the first time interval is 0.2 ms, and the rest intervals are all 0.1 ms.

It can be directly found that the larger the axis ratio, the faster the development of the interface. In the late time, Case 1 shows a trend of turbulent mixing, while Case 7 only has two big vortices which may correspond to the stage of the third image in Case 1. Furthermore, the structures of the interface in these seven cases are different, which may be ascribed to the baroclinic vorticity deposition mechanism. As depicted in Fig. 5, the larger the axis ratio, the bigger the misalignment of the pressure gradient with the density gradient and, therefore, the larger the baroclinic vorticity produced. Actually in the limit situation of $a = 0$, vorticity is only produced at the top and bottom of the ellipse, creating two opposing point vortices whose evolution can be described as a vortex pair, yielding a similar structure as in the bottom row of Fig. 4. Contrarily, in another limit case that $b = 0$, vorticity would be produced in two opposing horizontal and uniform vortex sheets, yielding similar images as in the top row of Fig. 4.

In Case 7 with the smallest axis ratio, the vorticity production is mainly concentrated at the upper and lower corners, which rolls up in time. Therefore, the development of this case is mainly driven by the corner vorticity and can be regarded as a big vortex-pair structure. As the axis ratio increases, the baroclinic vorticity production distributes at almost every position along the interface except the front and the rear parts. The increasing of the vorticity leads to a faster rolling up of vortices. In the largest ratio case (Case 1), due to the very big amount of vorticity produced along the very long interface, a second vortex develops in the big vortex at later time as indicated by dashed circles in Fig. 4. For this reason, we can consider this development as a bifurcation structure. We also noticed that from Cases 1–3 there are white areas attached to the main interface center in the early stage as denoted by 'S' in Fig. 4. This area is defined as a spike in Kumar et al. (2005) and is caused by shock focusing.

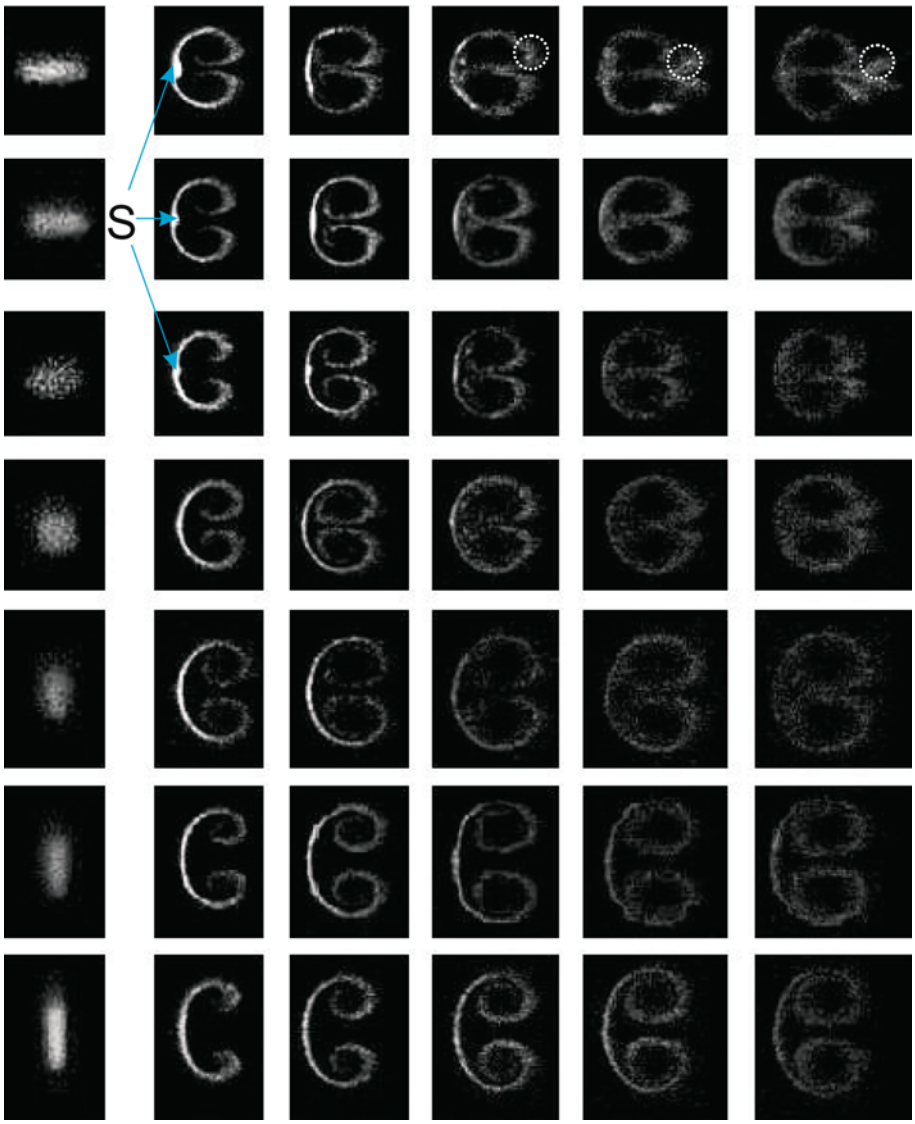

Fig. 4 Series dynamic images for all seven cases. Cases 1–7 correspond to the rows from *top* to *bottom*, respectively. The *first column* is the initial condition image, and the rest of the columns are dynamic images for evolution time at 0.2, 0.3, 0.4, 0.5 and 0.6 ms, respectively, after the passage of the incident shock wave

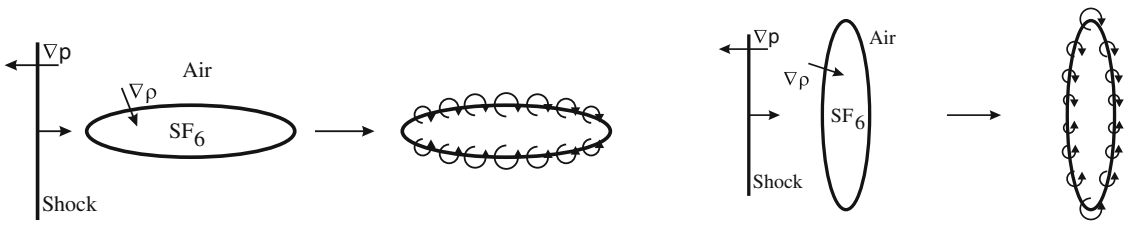

Fig. 5 The vorticity distribution produced by the interaction of a shock wave with an elliptic SF_6 cylinder in Case 1 (*left*) and Case 7 (*right*)

Then we further study the two typical elliptic cases, Cases 1 and 7, by comparing the geometrical sizes of the interface with that in the circular gas cylinder case as shown in Fig. 6. The geometrical sizes of the interface, i.e. the height of the cylinder h and the length of the cylinder l, are measured from Fig. 4. It can be found that the length of the cylinder trends to a same value after the initial impact and then deviates from

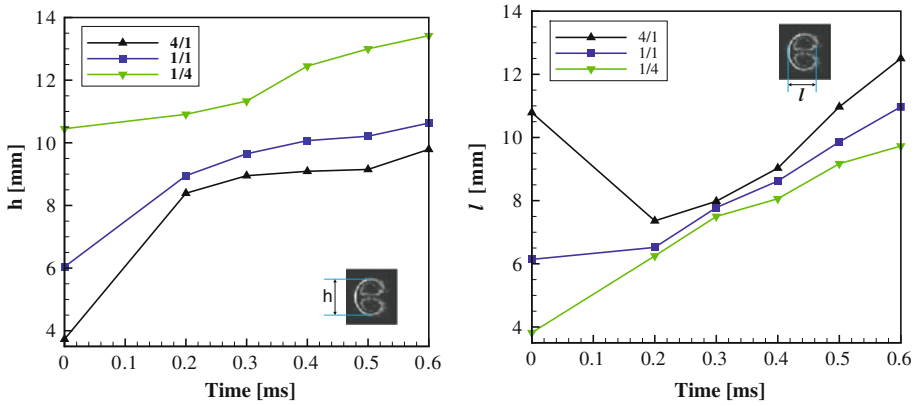

Fig. 6 Height (*left*) and length (*right*) for three axis ratios *a*/*b*: 4/1, 1/1 and 1/4

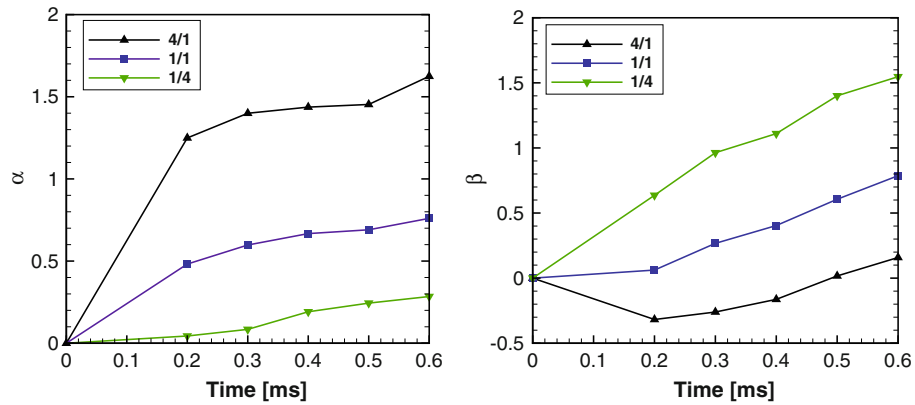

Fig. 7 Relative deformation in height (*left*) and length (*right*) for three axis ratios *a*/*b*: 4/1, 1/1 and 1/4

each other. Figure 7 shows the relative deformation α and β defined as $\alpha = (h - h_0)/h_0$ and $\beta = (l - l_0)/l_0$, respectively, with subscript '0' denoting the initial value. The increase of α in Case 1 is the fastest at the early stage and Case 7 is the slowest. This is related to the shock compression. Although the incident shock has the same strength, the traveling time of the transmitted shock is different due to the different shape of the cylinder, which leads to a different compression duration. The relative length behaves differently for three cases. In Case 1, the relative length decreases first due to the strong compression and then increases with time. In Case 7, the relative length increases linearly with time because the shock compression is very short.

4 Conclusions

The interaction of a planar shock with one elliptic heavy-gas (SF_6) cylinder surrounded by air is investigated experimentally. Seven elliptic cylinders with different aspect ratios are employed to study the influence of the initial shape on the evolution of the interface. These elliptic cylinders are different in axis ratio ranging from 4 to 0.25. All experiments are carried out in a shock tube with an incident shock Mach number of 1.25, and a high-speed camera combining with an initial camera is used to visualize the evolution of the interface.

It is found that the larger the axis ratio to the shock front, the faster and the severer the deformation of the gas cylinder. This may be ascribed to the baroclinic vorticity deposition mechanism. The larger the axis ratio, the bigger the misalignment of the pressure gradient with the density gradient and, therefore, the larger the baroclinic vorticity produced. In the smallest axis ratio case, the vorticity production is mainly concentrated at the upper and lower corners, which roll up in time. The development of this case is driven by the corner vorticity and can be regarded as a big vortex-pair structure. As the axis ratio increases, the baroclinic vorticity production distributes at almost every position along the interface except the front and the rear parts. The increasing of the vorticity leads to a faster rolling up of vortices. In the largest ratio case, due to

the very big amount of vorticity produced along the very long interface, a second vortex develops in the big vortex at later times. For this reason, we can consider this development as a bifurcation structure. We also noticed that for the very large axis-ratio cases there are white areas attached to the main interface center in the early stage.

Acknowledgments The authors would like to thank Prof. Jiming Yang for useful discussions during the course of this study. This research was carried out with the support of the National Natural Science Foundation of China under grants 10772166 and 10972144 the Science Foundation of China Academy of Engineering Physics (Grant No. 2008B0202011), and Defense Industrial Technology Development Program (Grant No. Z112009B004).

References

Arnett WD, Bahcall JN, Kirshner RP, Woosley SE (1989) Supernova 1987A. Annu Rev Astron Astrophys 27:629–700

Brouillette M (2002) The Richtmyer-Meshkov instability. Annu Rev Fluid Mech 34:445–468

Goodenough C, Kumar S, Marr-Lyon M, Boyts A, Prestridge K, Rightley P, Tomkins C, Cannon M, Kamm J, Rider W, Zoldi-Sood C, Orlicz G, Vorobieff P (2005) Planar velocity and scalar concentration measurements in shock-accelerated unstable fluid interfaces. Proc SPIE 5580:186–192

Haas JF, Sturtevant B (1987) Interaction of weak shock waves with cylindrical and spherical gas inhomogeneities. J Fluid Mech 181:41–76

Jacobs JW (1993) The dynamics of shock-accelerated light and heavy gas cylinders. Phys Fluids A 5:2239–2247

Kumar S, Orlicz G, Tomkins C, Goodenough C, Prestridge K, Vorobieff P, Benjamin R (2005) Stretching of material lines in shock accelerated gaseous flows. Phys Fluids 17:082107

Lindl DL, McCrory RL, Campbell EM (1992) Progress toward ignition and burn propagation in inertial confinement fusion. Phys Today 45:32–40

Markstein GH (1957) Flow disturbances induced near a slightly wavy contact surface, or flame front, traversed by a shock wave. J Aerosp Sci 24:238–239

Meshkov EE (1969) Instability of the interface of two gases accelerated by a shock wave. Fluid Dyn 4:101–104

Prestridge K, Vorobieff P, Rightley PM, Benjamin RF (2000) Validation of an instability growth model using particle image velocimetry measurements. Phys Rev Lett 84:4353–4356

Prestridge K, Rightley PM, Vorobieff P, Benjamin RF, Kurnit NA (2000) Simultaneous density-field visualization and PIV of a shock-accelerated gas curtain. Exp Fluids 29:339–346

Quirk JJ, Karni S (1996) On the dynamics of a shock-bubble interaction. J Fluid Mech 318:129–163

Richtmyer RD (1960) Taylor instability in shock acceleration of compressible fluids. Commun Pure Appl Math 13:297–319

Rightley PM, Vorobieff P, Benjamin RF (1997) Evolution of a shock-accelerated thin fluid layer. Phys Fluids 9:1770–1782

Rightley PM, Vorobieff P, Martin R, Benjamin RF (1999) Experimental observations of the mixing transition in a shock-accelerated gas curtain. Phys Fluids 11:186–200

Tomkins C, Kumar S, Orlicz G, Prestridge K (2008) An experimental investigation of mixing mechanisms in shock-accelerated flow. J Fluid Mech 611:131–150

Tomkins C, Prestridge K, Rightley P, Vorobieff P, Benjamin RF (2002) Flow morphologies of two shock-accelerated, unstable gas cylinders. J Vis 5:273–283

Tomkins C, Prestridge K, Rightley P, Marr-Lyon M, Vorobieff P, Benjamin RF (2003) A quantitative study of the interaction of two Richtmyer-Meshkov-unstable gas cylinders. Phys Fluids 15:986–1004

Zabusky N (1999) Vortex paradigm for accelerated inhomogeneous flows: visiometrics for the Rayleigh-Taylor and Richtmyer-Meshkov environments. Annu Rev Fluid Mech 31:495–536

Zoldi C (2002) A numerical and experimental study of a shock-accelerated heavy gas cylinder. PhD thesis, Department of Applied Mathematics, State University of New York at Stony Brook